



A Ground-based Near-ultraviolet Secondary Eclipse Observation of KELT-9b

Matthew J. Hooton¹, Christopher A. Watson¹, Ernst J. W. de Mooij², Neale P. Gibson¹, and Daniel Kitzmann³

¹Astrophysics Research Centre, School of Mathematics and Physics, Queen's University Belfast, Belfast BT7 1NN, UK; mhooton01@qub.ac.uk

²School of Physical Sciences, Dublin City University, Glasnevin, Dublin 9, Ireland

³University of Bern, Center for Space and Habitability, Gesellschaftsstrasse 6, CH-3012 Bern, Switzerland

Received 2018 September 28; revised 2018 December 5; accepted 2018 December 5; published 2018 December 14

Abstract

KELT-9b is a recently discovered exoplanet with a 1.49 day orbit around a B9.5/A0-type star. The unparalleled levels of ultraviolet irradiation that it receives from its host star put KELT-9b in its own unique class of ultra-hot Jupiters, with an equilibrium temperature >4000 K. The high quantities of dissociated hydrogen and atomic metals present in the dayside atmosphere of KELT-9b bear more resemblance to a K-type star than a gas giant. We present a single observation of KELT-9b during its secondary eclipse, taken with the Wide Field Camera on the Isaac Newton Telescope (INT). This observation was taken in the U -band, a window particularly sensitive to Rayleigh scattering. We do not detect a secondary eclipse signal, but our 3σ upper limit of 181 ppm on the depth allows us to constrain the dayside temperature of KELT-9b at pressures of ~ 30 mbar to 4995 K (3σ). Although we can place an observational constraint of $A_g < 0.14$, our models suggest that the actual value is considerably lower than this due to H^- opacity. This places KELT-9b squarely in the albedo regime populated by its cooler cousins, almost all of which reflect very small components of the light incident on their daysides. This work demonstrates the ability of ground-based 2 m class telescopes like the INT to perform secondary eclipse studies in the near-ultraviolet, which have previously only been conducted from space-based facilities.

Key words: planets and satellites: atmospheres – stars: individual (KELT-9) – techniques: photometric – ultraviolet: planetary systems

1. Introduction

The measurement of the drop in flux of an exoplanet–star pair when the planet is occulted by its host star has established itself as an important tool to study the atmospheres of exoplanets. At near-infrared (NIR) wavelengths and longer, thermal emission is the dominant source of flux from hot Jupiters (López-Morales & Seager 2007). Measurements of thermal emission have led to the detection of atmospheric features such as global heat redistribution (Knutson et al. 2007), the presence of a temperature inversion (Evans et al. 2017), and atmospheric variability (Armstrong et al. 2016).

At optical wavelengths and shorter, the component of flux from hot Jupiters due to thermal emission drops off sharply, such that the dominant component of flux is expected to be due to light reflected from its host. Measurements of thermal emission for various hot Jupiters imply that they should have reflection signatures that are sufficiently large so as to be detectable with current instrumentation (e.g., Schwartz & Cowan 2015; Schwartz et al. 2017). However, the vast majority of searches for reflected light from hot Jupiters at optical wavelengths—where their host stars typically emit most of their energy—have resulted in non-detections (e.g., Collier-Cameron et al. 2002; Leigh et al. 2003; Rowe et al. 2008; Gandolfi et al. 2013; Dai et al. 2017; Močnik et al. 2018). These results are consistent with predictions that scattering in the optical is suppressed by alkali absorption for cloud-free atmospheres (Sudarsky et al. 2000; Burrows et al. 2008).

To date, two studies have utilized the capabilities of *Hubble Space Telescope* (HST)/Space Telescope Imaging Spectrograph (STIS) to observe secondary eclipses of hot Jupiters in the near-ultraviolet (NUV). This wavelength range is potentially more favorable than the optical for detecting reflected light from exoplanets orbiting hot stars, as alkali absorption is much weaker and the Rayleigh scattering cross section is much higher. While Bell et al. (2017) did not detect reflected light at NUV wavelengths for WASP-12b ($T_{\text{eq}} \sim 2500$ K), Evans et al. (2013) measured a geometric albedo (A_g) of 0.40 ± 0.12 at 290–450 nm (a wavelength range overlapping with the U -band) for HD 189733 b ($T_{\text{eq}} \sim 1200$ K). These results support studies (e.g., Heng 2016; Stevenson 2016; Wakeford et al. 2017) suggesting that the most highly irradiated planets are less likely to have clouds in their atmospheres, as well as observational evidence for clouds in the atmosphere of HD 189733 b (Pont et al. 2008; Sing et al. 2011).

The 4050 K equilibrium temperature of the recently discovered KELT-9b (Gaudi et al. 2017) is by far the hottest of any known exoplanet. Its 1.49 day orbit around HD 195689, a B9.5/A0-type star, means that KELT-9b is more heavily irradiated at ultraviolet (UV) wavelengths than any other known exoplanet. Hoeijmakers et al. (2018) obtained high-resolution spectra of KELT-9b during its transit and detected Fe, Fe⁺, and Ti⁺ features with high significance, suggesting a temperature in excess of 4000 K at the terminator. The 4600 ± 150 K dayside temperature (Gaudi et al. 2017) measured from its z' -band eclipse depth (K. A. Collins et al. 2019, in preparation) is comparable to that of a K4-type star. This high dayside temperature means that KELT-9b is the only known planet that is expected to have a U -band eclipse depth >50 ppm due to thermal emission.

In this Letter we present a photometric ground-based U -band secondary eclipse of KELT-9b, which allows us to constrain the energy budget of this unique exoplanet. In Section 2 we



Original content from this work may be used under the terms of the [Creative Commons Attribution 3.0 licence](https://creativecommons.org/licenses/by/3.0/). Any further distribution of this work must maintain attribution to the author(s) and the title of the work, journal citation and DOI.

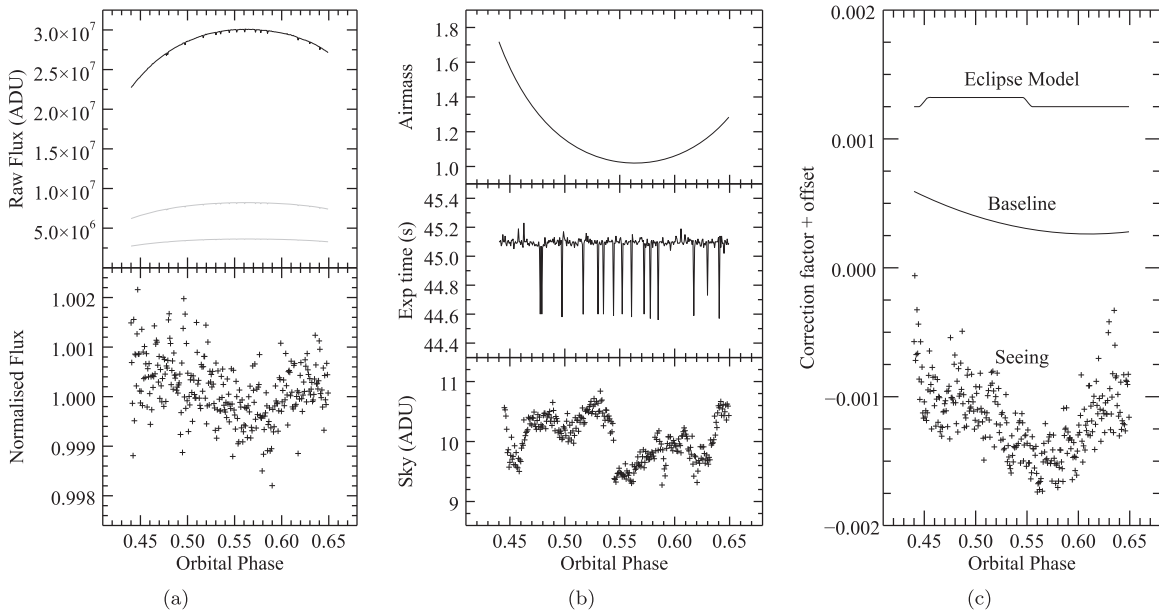


Figure 1. (a) Top panel: the raw light curves of KELT-9 (black points) and two comparison stars (gray points). Bottom panel: the normalized light curve prior to the MCMC fit. (b) A selection of parameters where no strong correlations were observed with the normalized light curve. (c) Components fitted to the normalized light curve using MCMC.

summarize our observation, in Section 3 we describe the steps taken to reduce the data, in Section 4 we describe how we fitted the eclipse depth, and in Section 5 we summarize how we modeled the KELT-9b spectrum and discuss our result, along with the wider implications of this study.

2. Observation

We observed one secondary eclipse of KELT-9b on 2017 July 20 using the Wide Field Camera (WFC) with the U -band filter on the 2.5 m Isaac Newton Telescope (INT) at the Observatorio del Roque de los Muchachos on the island of La Palma. The observations lasted ~ 8.3 hr and started at 21:15:29 UT. During this time, 326 frames were obtained with an average cadence of 75.1 s and an exposure time of 45.1 s. 155 of these frames were taken when KELT-9b was fully or partially occulted by its host. The observations commenced and concluded in evening and morning twilights, respectively. 32 frames taken during twilight, when KELT-9b was out of eclipse, were removed as the increased sky brightness caused strong systematics in those sections of the light curves. For 17 frames that were randomly distributed through the night, we observed that the exposure time was only ~ 44.6 s. However, due to our use of differential photometry, no visible correlation was observed between exposure time and flux once the target had been normalized with the comparison stars. Although the WFC consists of a four-charge-coupled-device (CCD) mosaic—each with a pixel scale of $0''.33$ per pixel—only the central CCD (CCD4) was used, giving us a field of view of $\sim 22''.7$ by $11''.4$.

We performed the observations with the telescope defocused, which acts to reduce overheads, minimize errors associated with flat-fielding, and make the resulting point-spread functions (PSFs) less sensitive to variations in seeing. This resulted in a donut-shaped PSF with a diameter of 54 pixels ($18''$). Due to the defocusing, the telescope auto-guider was not used. Instead, a custom code that uses the science frames to account for telescope drift was used. Care was taken

to ensure that the target and the most promising comparison stars were positioned on well-behaved parts of the detector and the drift throughout the night was less than four pixels ($1''.3$).

3. Data Reduction

Each of the images was overscan-subtracted on a row-by-row basis using the mean of the overscan regions at either side of the CCD. The row by row bias subtraction was used to correct for a known issue with the WFC that affected about half of the frames, in which the bias level present in the frames drops and corrects itself after a period of time. This was followed by a full-frame bias subtraction. The images were then each flat-fielded using a master flat constructed from twilight flats. Finally, a second-order polynomial was fit to and subtracted from the entirety of each frame with the stars masked, to remove the small gradient in the sky background across the CCD.

We observed crosstalk between the four CCDs that make up the WFC mosaic, which caused bright stars from one CCD to be ghosted onto the same position on other CCDs. This caused the addition or subtraction of <3 ADU on a background of ~ 2000 ADU in the raw frames. However, the target and comparison stars did not fall on any of the affected regions.

Finally, we performed aperture photometry on the target and each of the two comparison stars using an aperture with a radius of 51 pixels, selected to maximize the flux and minimize the influence from the background. The annuli used to subtract the residual sky background from each star had inner and outer radii of 72 and 91 pixels, respectively.

4. Analysis and Results

The raw light curves for the target and each of the comparison stars are shown in the top panel of Figure 1(a). The two comparisons (HD 195558 and BD+39 4224) are both A-type stars and have median fluxes of 0.27 and 0.12, respectively, relative to KELT-9 throughout the observation. The light curve in the bottom panel of Figure 1(a) was created

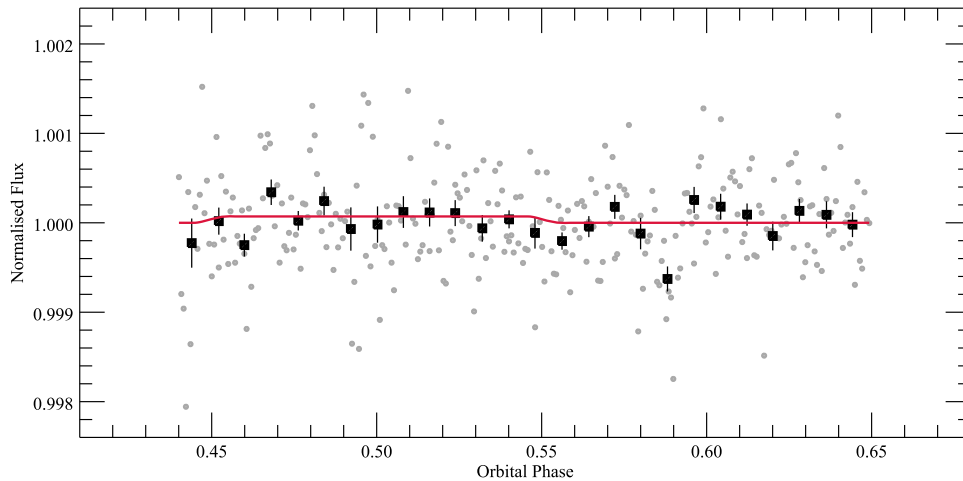


Figure 2. Unbinned normalized light curve (gray points) after decorrelating with seeing and a second-order polynomial, and the best-fit eclipse model (red line). The data binned by phase 0.008 (black squares) are shown for clarity.

by dividing the target light curve by the sum of the two comparison light curves and normalizing for a median value of 1. This step removed visible correlations with airmass and exposure time (top and middle panels of Figure 1(b)) that were visible in the raw light curves. No correlations were observed with the x and y positions of the stars on the detector. There were small discontinuities visible in the sky background levels for the target (see the bottom panel of Figure 1(b)) and comparison stars, but no such features were visible in the corresponding light curves. On initial inspection, a dip in the sky background at phase of ~ 0.59 corresponded with a dip in flux in the normalized light curve (also see Figure 2). However, the latter feature was found to be much broader and no significant correlation was found. Despite our method of defocusing the telescope, a strong correlation with seeing was visible. There was also a low-order trend present throughout the time-series that was not removed by the normalization with the comparison stars.

We fit for each of these trends simultaneously with an eclipse model using a Markov Chain Monte Carlo (MCMC) method with the Metropolis–Hastings algorithm and orthogonal stepping. To model the eclipse, we used the Mandel and Agol transit model (Mandel & Agol 2002) with the limb-darkening coefficients set to zero. The relevant stellar, planetary, and orbital parameters were all fixed using values from Gaudi et al. (2017), which are shown in Table 1. The trend in the baseline was modeled using a second-order polynomial, which optimized the Bayesian information criterion with respect to higher- and lower-order models. The time-dependent and time-independent components of the noise associated with the residual flux were measured using the wavelet method (Carter & Winn 2009). We ran an MCMC where the components of the model associated with the eclipse depth, a linear function of seeing, the polynomial baseline and the wavelet noise parameters were all allowed to vary. First, we ran a “burn-in” phase of 10^5 steps, where the step sizes were recalculated every 10^4 steps to set proportionate step sizes for each parameter. We then used these step sizes in an MCMC chain of 10^6 steps to get the best fit values for each parameter, which are shown in Figure 1(c). We verified convergence by checking the Gelman–Rubin criterion (Gelman & Rubin 1992).

The detrended light curve is shown in Figure 2, with the best-fit eclipse model shown in red. While a negative value for

Table 1
Parameters of the KELT-9 System

Parameter	Value	References
Stellar Parameters		
R_* (R_\odot)	$2.362^{+0.075}_{-0.063}$	A
T_* (K)	$10,170 \pm 450$	A
$\log(g)$	4.091 ± 0.014	A
[Fe/H]	-0.03 ± 0.20	A
Planetary Parameters		
R_p (R_J)	$1.888^{+0.062}_{-0.052}$	A
t_0 (MJD)	57095.18572 ± 0.00014	A
P (days)	1.4811235 ± 0.0000011	A
a (au)	$0.03462^{+0.0110}_{-0.0093}$	A
i ($^\circ$)	86.79 ± 0.25	A
T_{day} (K)	4600 ± 150	A
$F_{\text{ecl},z'}$ (ppm)	1006 ± 97	B
Measured Parameters		
$F_{\text{ecl},U}$ (ppm)	-71 ± 84	C
$F_{\text{ecl},U}$ (ppm)	<181 (3σ limit)	C
T_{day} (K)	<4995 (3σ limit)	C
σ_w	$(3.32 \pm 0.11) \times 10^{-4}$	C
σ_r	$(0.7 \pm 5.6) \times 10^{-4}$	C

References. (A) Gaudi et al. (2017), (B) K. A. Collins et al. (2019, in preparation), (C) this work.

a secondary eclipse depth is unphysical, we allowed this to avoid biasing the MCMC fit. The best fit depth of -71 ± 84 ppm allowed us to place an upper limit on the secondary eclipse depth of 181 ppm at 3σ .

5. Discussion and Conclusions

We jointly interpreted our U -band upper limit and the z' -band eclipse detection (K. A. Collins et al. 2019, in preparation) by generating high-resolution emission spectra with wavenumber resolution of 0.03 cm^{-1} (left panel of Figure 3; shown in 2 nm wavelength bins for clarity), which were calculated using a four-stream discrete ordinate radiative transfer method. For the temperature–pressure (TP) profiles (Figure 3, right panel) we used the approximations for an irradiated atmosphere from Guillot (2010), with an infrared (IR) opacity of $0.03 \text{ cm}^2 \text{ g}^{-1}$.

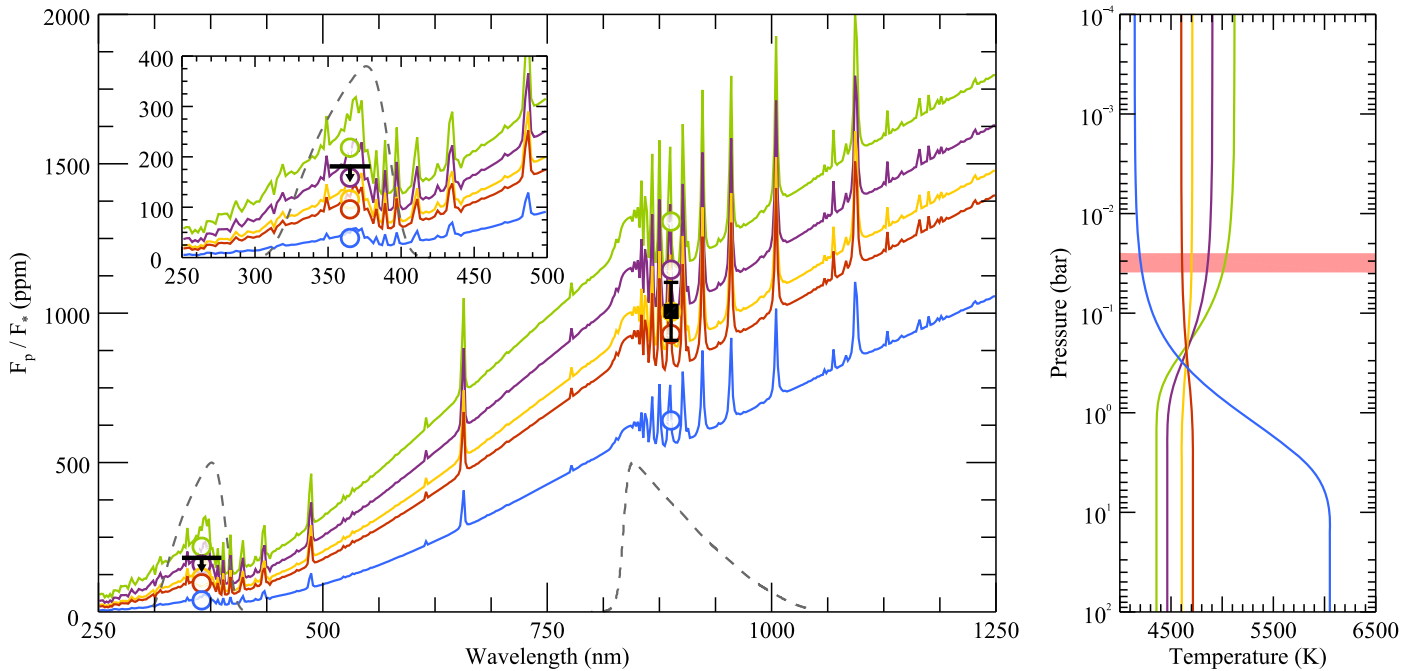


Figure 3. Left panel: model spectra for the five temperature profiles shown in the right panel, incorporating flux associated with both thermal emission and scattering. Our U -band upper limit and the z' -band eclipse depth (K. A. Collins et al. 2019, in preparation) are shown in black and the expected eclipse depths for each profile are marked with colored data points. The response functions associated with the two bandpasses are marked with gray dashed lines. A close-up of U -band wavelengths is shown inset. Right panel: temperature–pressure profiles for each of the spectra shown. The red shaded area shows the pressure levels from which the thermal emission for all the models originate, when approximated as blackbodies.

The ratio of the shortwave to the IR opacity (γ), which effectively controls the shape of the TP profile, is treated as a free parameter. Strong absorption of shortwave radiation in the upper atmosphere can result in large temperature inversions of several hundreds of Kelvin, which has previously been demonstrated for species such as TiO and VO (Spiegel et al. 2009). Atomic and ionic species expected to be present in the atmosphere of KELT-9b (such as Fe and Fe⁺; Hoeijmakers et al. 2018) are strong absorbers at optical and shorter wavelengths. Hence, the five spectra shown in Figure 3 were selected to explore a range of possible TP profiles, ranging from a strong inversion ($\gamma = 2$) to a rapid decrease in temperature with altitude ($\gamma = 0.2$). As KELT-9b is tidally locked and expected to inefficiently redistribute heat from dayside to nightside, the temperatures in all five profiles are well above the equilibrium temperature of 4050 K from Gaudi et al. (2017). The chemical composition is calculated using the `FastChem` equilibrium chemistry code (Stock et al. 2018), assuming solar elemental abundances. As shown by Kitzmann et al. (2018), the assumption of chemical equilibrium is reasonable for the hot dayside of KELT-9b.

We account for about 50 different gaseous absorbers in the atmosphere. Cross sections for CO and H₂O were calculated with the opacity calculator `HELIOS-K` (Grimm & Heng 2015), using the corresponding Exomol line lists. Atoms and ions, including Fe, Fe⁺, Ti, Ti⁺, Ca, and Ca⁺, are incorporated with line list data from the Kurucz database. Continuum absorption of H⁻ is treated according to John (1988). Additionally, we include the collision-induced absorption of H₂–H₂, H₂–He, and H–He pairs, based on data from HITRAN. Furthermore, Rayleigh scattering of H₂, H, He, and CO is incorporated in the radiative transfer calculations as well.

For KELT-9, we used a spectrum for a 10,000 K star with $\log(g) = 4$ and $[\text{Fe}/\text{H}] = 0$ (based on values from Gaudi et al. 2017,

Table 2
Description of Spectra in Figure 3

Color	γ	$F_{\text{ecl},U}$ (ppm)	$F_{\text{ecl},z'}$ (ppm)	T_B (K)
Green	2.0	218	1307	5080
Purple	1.5	159	1146	4890
Yellow	1.1	116	1005	4700
Red	0.9	96	930	4600
Blue	0.2	39	641	4165

shown in Table 1) from the NextGen Model grid of theoretical spectra (Hauschildt et al. 1999).

We integrated each of the spectra over both filter response functions, which incorporate atmospheric extinction and the quantum efficiency of the detectors, in order to calculate the expected eclipse depths for each value of γ in each band. These are shown on the left panel of Figure 3 and listed in Table 2. The effective midpoint of the U -band response function falls at shorter wavelengths than the Balmer jump of KELT-9, boosting the expected eclipse depths in this bandpass. At low resolution for the wavelengths shown, the spectrum associated with each TP profile is almost indistinguishable from that of a blackbody spectrum, with the majority of the features visible in the left panel of Figure 3 originating in the stellar spectrum. This is due the high atmospheric mixing ratio of H⁻ ions: a major source of opacity at NUV, optical, and NIR wavelengths (John 1988) that atmospheric models for other ultra-hot Jupiters predict will be present in large quantities (e.g., Arcangeli et al. 2018; Lothringer et al. 2018). The brightness temperatures for the blackbody spectra most closely matching each of our spectra are also listed in Table 2.

When comparing the brightness temperatures for each spectrum to their corresponding TP profiles, it is apparent that each of these temperatures originates at pressure levels of

~ 30 mbar (right panel of Figure 3; shaded red), independently of the form taken by each of the TP profiles. Thus, we use our result to place a 3σ limit of 4995 K on the dayside temperature of KELT-9b at pressure levels of ~ 30 mbar, which is in agreement with the value 4600 ± 150 K in Gaudi et al. (2017). While two broadband eclipse measurements cannot place strong constraints on the form the TP profile of KELT-9b takes at these altitudes, they tentatively favor profiles without a strong temperature inversion. However, the two measurements combined support the theory that the continuum of H^- opacity produces an emission spectrum that is very similar to a blackbody at these wavelengths.

When adopting the temperature of 4600 ± 150 K for the altitudes probed by our observations, we can use our U -band observational data to place a 3σ limit of $A_g < 0.14$. Our models show that the main source of scattering in the NUV is molecular Rayleigh scattering. However, this is expected to be negligible compared to H^- extinction in the dayside of KELT-9b. Kitzmann et al. (2018) predicted that free electrons are present in significant quantities in the upper atmosphere of KELT-9b, but that the cross section of Thomson scattering is too small to have a significant contribution to the total flux. When only considering flux from reflected light, integrating over the U -band response function yields predicted eclipse depths of ~ 3 ppm for all of the TP structures shown, corresponding to an A_g of ~ 0.005 . Hence, the flux due to reflected light is expected to be negligible compared to the thermal emission in the U -band and well below the detection limits of our observation.

Of the two hot Jupiters for which similar measurements have been carried out, this study suggests that the reflective properties of KELT-9b are more comparable to those of WASP-12b than HD 189733 b. This fits into the wider picture of other hot Jupiters for which a measurement of geometric albedo has been performed, with the vast majority of studies measuring very small components of incident light reflected. This in turn supports studies that suggest that the temperatures present in the daysides of ultra-hot Jupiters are too high for condensates to form. Further secondary eclipse observations in the NUV and blue-optical of HD 189733 b and other hot Jupiters with lower levels of irradiation are required to assess the validity of claims that cloudiness (and therefore observed Rayleigh scattering) scales with temperature in the daysides of hot Jupiters.

Full phase-curve observations with space-based facilities such as *Spitzer*, the *CHAracterising ExOPlanet Satellite (CHEOPS)*, and the *Transiting Exoplanet Survey Satellite (TESS)* will put tighter constraints on the energy budget of KELT-9b and help to break the degeneracy between Bond albedo and atmospheric circulation. Transmission spectroscopy observations at blue-optical wavelengths will test the occurrence of Rayleigh scattering and test how the reflective properties of KELT-9b vary with longitude. Further secondary eclipse observations at optical and IR wavelengths will put tighter constraints on the spectral energy distribution of KELT-9b.

This Letter demonstrates the ability of ground-based 2 m class telescopes like the INT to perform secondary eclipse observations for hot Jupiters in an age where there will be no space-based alternatives, enabling the placement of a tight constraint on the UV eclipse depth from a single observation. For cooler exoplanets than KELT-9b, this will be a direct

measurement of their geometric albedos. To date, all previous studies to detect reflected light from transiting exoplanets have been conducted using space-based facilities such as *Hubble*, *Kepler* (e.g., Kipping & Spiegel 2011), *Convection, Rotation and planetary Transits (CoRoT)*; Snellen et al. 2010), and *Microvariability and Oscillations of STars (MOST)*; Rowe et al. 2008). Currently, the only suitable⁴ space-based facility with NUV coverage is *Hubble*, which is likely to permanently go out of operation in the next decade. Although *Hubble* does not suffer the light extinction in the NUV that ground-based facilities do, the lower time-pressure on ground-based facilities enables the easier acquisition of several secondary eclipses, which would yield even higher photometric precision than our single observation.

We thank the anonymous referee for their full and thorough feedback. We are grateful to the staff of the INT for their assistance with these observations. The INT is operated on the island of La Palma by the Isaac Newton Group of Telescopes in the Spanish Observatorio del Roque de los Muchachos of the Instituto de Astrofísica de Canarias. M.J.H. acknowledges funding from the Northern Ireland Department for the Economy. C.A.W. acknowledges support from STFC grant ST/P000312/1. N.P.G. acknowledges support from the Royal Society in the form of a University Research Fellowship. D.K. acknowledges financial and administrative support by the Center for Space and Habitability and the PlanetS National Centre of Competence in Research (NCCR).

ORCID iDs

Matthew J. Hooton  <https://orcid.org/0000-0003-0030-332X>

Ernst J. W. de Mooij  <https://orcid.org/0000-0001-6391-9266>

Neale P. Gibson  <https://orcid.org/0000-0002-9308-2353>

Daniel Kitzmann  <https://orcid.org/0000-0003-4269-3311>

References

- Arcangeli, J., Desert, J.-M., Line, M. R., et al. 2018, *ApJL*, 855, L30
 Armstrong, D. J., de Mooij, E., Barstow, J., et al. 2016, *NatAs*, 1, 0004
 Bell, T. J., Nikolov, N., Cowan, N. B., et al. 2017, *ApJL*, 847, L2
 Burrows, A., Budaj, J., & Hubeny, I. 2008, *ApJ*, 678, 1436
 Carter, J. A., & Winn, J. N. 2009, *ApJ*, 704, 51
 Collier-Cameron, A., Home, K., Penny, A., & Leigh, C. 2002, *MNRAS*, 330, 187
 Dai, F., Winn, J. N., Yu, L., & Albrecht, S. 2017, *AJ*, 153, 40
 Evans, T. M., Pont, F., Sing, D. K., et al. 2013, *ApJL*, 772, L16
 Evans, T. M., Sing, D. K., Kataria, T., et al. 2017, *Natur*, 548, 58
 Gandolfi, D., Parviainen, H., Fridlund, M., et al. 2013, *A&A*, 557, A74
 Gaudi, B. S., Stassun, K. G., Collins, K. A., et al. 2017, *Natur*, 546, 514
 Gelman, A., & Rubin, D. B. 1992, *StSc*, 7, 457
 Grimm, S. L., & Heng, K. 2015, *ApJ*, 808, 182
 Guillot, T. 2010, *A&A*, 520, A27
 Hauschildt, P. H., Allard, F., & Baron, E. 1999, *ApJ*, 512, 377
 Heng, K. 2016, *ApJL*, 826, L16
 Hoeijmakers, H. J., Ehrenreich, D., Heng, K., et al. 2018, *Natur*, 560, 453
 John, T. L. 1988, *A&A*, 193, 189
 Kipping, D. M., & Spiegel, D. S. 2011, *MNRAS*, 417, L88
 Kitzmann, D., Heng, K., Rimmer, P. B., et al. 2018, *ApJ*, 863, 183
 Knutson, H. A., Charbonneau, D., Allen, L. E., et al. 2007, *Natur*, 447, 183
 Leigh, C., Collier-Cameron, A., Home, K., Penny, A., & James, D. 2003, *MNRAS*, 344, 1271
 López-Morales, M., & Seager, S. 2007, *ApJL*, 667, L191
 Lothringer, J. D., Barman, T., & Koskinen, T. 2018, *ApJ*, 866, 27

⁴ The *XMM-Newton* Optical Monitor (Mason et al. 2001) has NUV coverage, but the instrument is designed to supplement simultaneous X-ray observations.

- Mandel, K., & Agol, E. 2002, [ApJL](#), **580**, L171
- Mason, K. O., Breeveld, A., Much, R., et al. 2001, [A&A](#), **365**, L36
- Močnik, T., Hellier, C., & Southworth, J. 2018, [AJ](#), **156**, 44
- Pont, F., Knutson, H., Gilliland, R. L., Moutou, C., & Charbonneau, D. 2008, [MNRAS](#), **385**, 109
- Rowe, J. F., Matthews, J. M., Seager, S., et al. 2008, [ApJ](#), **689**, 1345
- Schwartz, J. C., & Cowan, N. B. 2015, [MNRAS](#), **449**, 4192
- Schwartz, J. C., Kashner, Z., Jovmir, D., & Cowan, N. B. 2017, [ApJ](#), **850**, 154
- Sing, D. K., Pont, F., Aigrain, S., et al. 2011, [MNRAS](#), **416**, 1443
- Snellen, I. A. G., de Mooij, E. J. W., & Burrows, A. 2010, [A&A](#), **513**, A76
- Spiegel, D. S., Silverio, K., & Burrows, A. 2009, [ApJ](#), **699**, 1487
- Stevenson, K. B. 2016, [ApJL](#), **817**, L16
- Stock, J. W., Kitzmann, D., Patzer, A. B. C., & Sedlmayr, E. 2018, [MNRAS](#), **479**, 865
- Sudarsky, D., Burrows, A., & Pinto, P. 2000, [ApJ](#), **538**, 885
- Wakeford, H. R., Visscher, C., Lewis, N. K., et al. 2017, [MNRAS](#), **464**, 4247